Inorganic Chemistry

Article

pubs.acs.org/IC

Structure and Redox Behavior of Iron Oxophlorin and Role of Electron Transfer in the Heme Degradation Process

Mahin Gheidi, Nasser Safari,* and Mansour Zahedi

Department of Chemistry, Faculty of Sciences, Shahid Beheshti University, G. C., Evin, 19839-63113, Tehran, Iran

Supporting Information

ABSTRACT: Iron-oxophlorin is an intermediate in heme degradation, and the metal oxidation number can alter spin, electron distribution, and the reactivity of the metal and the oxophlorin ring. The role of electron transfer in the structure and reactivity of $[(Py)_2Fe^{III}(PO)]$ (PO is the oxophlorin trianion) in different redox states has been investigated using the B3LYP and OPBE methods with the 6-31+G* and 6-311+G** basis sets. A computation study has shown that $[(py)_2\ Fe^{III}(PO)]$ loses one electron from its a_{2u} orbital. Thus the oxidized species, $[(Py)_2Fe^{III}(PO^{\bullet})]^+$ (where $PO^{\bullet}$ is the oxophlorin dianion radical), has an open-shell-singlet ground state with a $d_{xy}^{\ 2}\ d_{xz}^{\ 2}\ a_{2u}^{\ 1}\ d_{yz}^{\ 1}$ electronic configuration with closely lying triplet and quintet states which are populated at ambient temperature. The aforementioned complex is highly reactive toward O_2. The reduced species $[(Py)_2Fe^{II}(POH)]$ (where POH is the hydroxyheme) has the closed-shell-singlet ground state $(\pi_{xz}\ \pi_{yz})^4\ a_{2u}^{\ 2}\ d_{xy}^{\ 2}$ electronic configuration in which pyridines have a more π-accepting character and, thus, are tightly bound to iron. This reduced form is considerably less reactive toward O_2. The axial ligands effects (Im, *t*-BuNC) have also been studied in redox reactions of iron oxophlorin complexes. Complex $[(Im)_2Fe^{III}(PO)]$ shows facile oxidation to form a cation radical and a reduction to form hydroxy while the $[(t\text{-BuNC})_2Fe^{II}(PO^{\bullet})]$ has high positive oxidation potential.

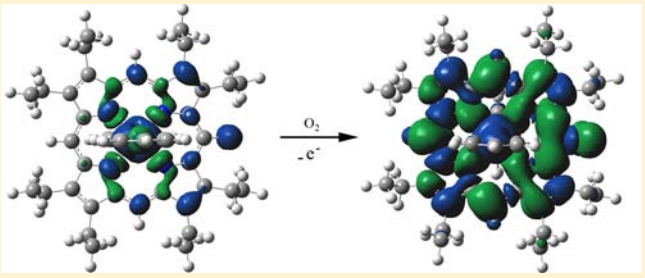

INTRODUCTION

Heme catabolism is an important physiological process that is carried out by O_2/NADPH in the presence of heme oxygenase enzyme/HO in animals and birds. Heme oxygenase performs the essential role of destroying unwanted heme.[1−6] The coupled oxidation in which heme degradation occurs via O_2/reducing agent in a coordinating solvent has been widely used as a model for biological heme catabolism.[7−9] Three major intermediates isolated and characterized in this heme oxygenase process or in a coupled oxidation model system are α-hydroxyheme, oxophlorin, and verdoheme,[7,10−14] Scheme 1.

It is known that oxophlorin is air sensitive and in the presence of O_2 transforms to verdoheme by releasing carbon monoxide. Balch and co-workers have indeed characterized complexes of oxophlorin macrocycles in model systems called coupled oxidation.[15−20] Conversion of heme to biliverdin has been specially studied in biological[21−24] and theoretical[25−29] systems. The mechanism that converts oxophlorin into verdoheme is, however, the least known step, and especially the role of electron transfer in this process is the subject of challenges. Different pathways have been proposed for the conversion of iron oxophlorin to iron verdoheme. In one proposed path, the iron oxophlorin reacts with O_2 and one electron simultaneously.[30] There is another proposed path in which O_2 alone converts α-meso-hydroxyheme to ferric verdoheme and that one electron is used to reduce the ferric verdoheme to the ferrous species.[31,32] In the third proposition, conversion of oxophlorin to ferrous verdoheme requires only oxygen molecules that act as the macrocycle oxidant and as a reactant with the oxophlorin ring. This path is specially supported by a very low potential that interconverts $[(Py)_2Fe^{III}(OEPO)]$ (where OEPO is the octaethyloxophlorin trianion) and $[(Py)_2Fe^{III}(OEPO^{\bullet})]^+$ (where $OEPO^{\bullet}$ is the octaethyloxophlorin dianion radical).[16]

Therefore, the questions of whether the iron oxophlorin complex requires additional electrons before reacting with dioxygen to yield verdoheme or if the oxidation of the iron oxophlorin ring by dioygen is a prerequisite for conversion to iron verdoheme remain to be resolved. For understanding the mechanism of conversion of the oxophlorin macrocycle to verdoheme, the first essential step is the exact determination of the reactive macrocycle in oxophlorin states. Recently, we have demonstrated how the electronic configuration, oxidation, spin states, and reactivity in $[L_2Fe(PO)]$ can be altered when the axial ligation changes.[33] In this article, redox reactions of iron oxophlorins $[L_2Fe(PO)]$ have been investigated, and the oxidized and reduced intermediates and their reactivity in the oxidized destruction of heme have been identified.

METHODS

We employed density functional theory methods[34] as implemented in the Gaussian 2003 (A.B.3) program series.[35] OPBE and B3LYP methods[36,37] and 6-31+G* and 6-311+G**

Received: August 8, 2012
Published: November 12, 2012

   dx.doi.org/10.1021/ic3017497 | Inorg. Chem. 2012, 51, 12857−12866

Scheme 1

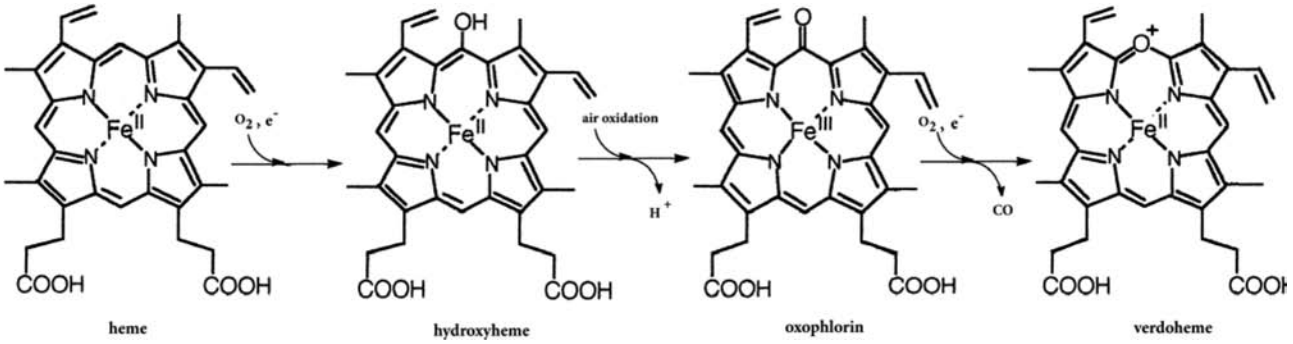

Table 1. Calculated Relative Energies for All of Compounds Using OPBE/6-311+G** Methods (Energy Stabilization (kcal mol^{-1}))

	OPBE				B3LYP			
compounds	singlet (closed-shell)	singlet (open-shell)	triplet	quintet	singlet (closed-shell)	singlet (open-shell)	triplet	quintet
$[(Py)_2Fe^{III}(PO^{\bullet})]^{+\,a}$	5.43	0.00	0.82	1.96	4.89	0.00	1.05	2.22
$[(Py)_2Fe^{III}(PO^{\bullet})]^{+\,b}$	6.22	0.50	0.75	1.28	6.60	1.45	1.80	2.38
$[(Py)_2Fe^{III}(PO^{\bullet})]^{+\,c}$	13.50	0.00	1.35	3.22	12.71	0.00	1.89	3.65
$[(Py)_2Fe^{II}(POH)]^{a}$	1.12		12.41		0.00		8.50	
$[(Py)_2Fe^{II}(POH)]^{b}$	0.00		9.72		0.50		7.92	

[a]Stands for when pyridines are in the perpendicular plane. [b]Stands for when pyridines are in the common plane. [c]Stands for when complex is in the solvent of H_2O.

basis functions[38,39] have been used in this investigation. The OPBE/6-31+G* method is used for the optimization of all structures, and in all cases, the energy was correct by single point calculation with a larger basis set 6-311+G** for all atoms. It is well-known that the 6-31+G* basis set tends to predict high-spin states at energies which are too low. The spin unrestricted versions of the B3LYP (UB3LYP with the command guess=mix) and OPBE methods were applied even to singlet states when the reaction species were reasonably considered to have an open-shell-singlet electronic configuration.[40−44] In the open-shell singlet, where S sets to zero, the pop analyses were performed, and then the geometry was relaxed by starting an optimization in this state. For complex $[(Py)_2Fe^{III}(PO^{\bullet})]^{+}$, in the open-shell singlet spin state where its spin contamination is so significant, there is the possibility of contribution to an admixture of triplet spin state. To account for spin contamination, a correction based on the expectation value of S^2 calculated over the Kohn−Sham determinants was used even though these determinants are not eigenvalues of the S^2 operator. Subtraction of the energy contribution of the higher spin states, E_{s+1}, from the spin contaminated energy, E_C, and renormalization yields an estimate of the energy of the desired pure spin state, E_s, as follows:[45,46]

$$a = \frac{\langle S^2\rangle_C - s(s+1)}{2(s+1)}$$

$$E_S = \frac{E_C - aE_{s+1}}{1-a}$$

A subsequent analytical frequency calculation characterized the structures as local minima with real frequencies only. All energies reported in this work use the latter basis set and are corrected for zero-point energies as taken from the frequency calculations.

We corrected the gas-phase energies using the self-consistent reaction field (SCRF) model[47] implemented with the 6-31+G* basis set at the solvent-phase geometry. The two solvents were specified by dielectric constant (ε), that is, ε = 37.5 for acetonitrile and ε =78.5 for water. The solvation calculations do not take into consideration any ion pairing or the effects of the counterions. Inclusion of counterions will make the calculation much too complicated and time-consuming and, therefore, impractical.

Atomic charge and spin density studies are based on Mulliken calculation. The natural bond orbital (NBO) analysis is used to explain electrons in the d orbitals of iron and the macrocycle ring as well as to assign the atomic charges. The molecular orbital analyses have been performed by Gauss View applied to the respective Gaussian output file.

RESULTS AND DISCUSSION

Due to the resemblance of the heme−HO complex to myoglobin, some authors have assumed that the ferric heme iron in the heme−HO complex at neutral pH is six-coordinate.

The model of the oxophlorin site of six coordinates used in DFT calculations is an iron oxophlorin complex taken from the crystal structure of the iron complex of octaethyloxophlorin[16,48] after substituting the ethyl group with hydrogen, abbreviated as PO.

In previous studies,[33] we showed that complex $[(Py)_2Fe^{III}(PO)]^0$ has two possible alternative electronic configurations, $\pi_{xz}^2\,\pi_{yz}^2\,a_{2u}^2\,d_{xy}^1$ and $\pi_{xz}^2\,\pi_{yz}^2\,d_{xy}^2\,a_{2u}^1$; these were labeled as $^2[(Py)_2Fe^{III}(PO)]^0_{xy}$ and $^2[(Py)_2Fe^{II}(PO^{\bullet})]^0_{a_{2u}}$ respectively. Therefore, it was proposed that $^2[(Py)_2Fe^{II}(PO^{\bullet})]^0_{a_{2u}}$ could be more reactive toward O_2.

In this work, the reduced and oxidized forms of $[(L)_2Fe^{III}(PO)]$, L = Py, Im, and *t*-BuNC, have been investigated in all possible spin states. The oxidation and reduction potential of the $[(L)_2Fe^{III}(PO)]^0$ and the

dx.doi.org/10.1021/ic3017497 | Inorg. Chem. 2012, 51, 12857−12866

$[(L)_2Fe^{III}(PO)]^+$ and $[(L)_2Fe^{II}(POH)]$ species have been also studied. For all complexes, OPBE predicts the correct spin ground state. Furthermore, in a series of papers, Ghosh and coworkers[49−51] have clearly demonstrated that OPBE seems to give good results, not only for iron complexes but also for other transition metals.

Table 1 shows the computed relative stabilization energy for these compounds. The details of the bond distances for all compounds via the OPBE method are given in Table 2, and the optimized structures are presented in the Supporting Information. Charge densities and spin distributions for all compounds are presented in Table 3.

Table 2. Selected, Calculated Bond Distances for Iron Oxophlorin Complexes Using the OPBE/6-31+G* Method

compound	Fe−N_{ax}	Fe−$N_{ave.ring}$	C−O
$[(Py)_2Fe^{III}(PO^{\bullet})]^+$			
singlet	2.06	2.00	1.25
triplet	2.06	2.00	1.27
quintet	2.28	2.00	1.27
$[(Py)_2Fe^{III}(PO)]^0$			
doublet	2.03	2.02	1.27
quartet	2.31	2.01	1.27
sextet	2.28	2.08	1.27
$[(Py)_2Fe^{II}(POH)]$			
singlet	2.01	2.00	1.40
triplet	2.36	2.01	1.40

$[(Py)_2Fe^{III}(PO^{\bullet})]^+$. The structure of six-coordinate $[(Py)_2Fe^{III}(PO^{\bullet})]^+$ has been fully optimized and computed with the pyridine groups in parallel and perpendicular planes in all possible spin states using the OPBE and B3LYP/6-31+G* methods. All spin state potential energy surfaces are close in $[(Py)_2Fe^{III}(PO^{\bullet})]^+$: for example, the open-shell, antiferomagnetically coupled, singlet state is the ground state accompanied with a very low lying, feromagnetically coupled, triplet state. The triplet and quintet states are only 0.82 and 1.96 kcal/mol higher in energy than the open-shell singlet ground state, while the closed-shell singlet state is 5.43 kcal/mol higher in energy than the open-shell-singlet state at the OPBE/6-311+G** level. In aqueous media, the energy difference between the open-shell singlet ground state and closed-shell singlet state is increased to 13.50 kcal/mol. Therefore, in polar solvents, two antiferromagnetically coupled electrons in iron and macrocycles insert more polar character into the $^1[(Py)_2Fe^{III}(PO^{\bullet})]^+$ (open-shell) and make it more stabilized. The electronic configuration for both open shell singlet and triplet states is $d_{xy}^2\, d_{xz}^2\, a_{2u}^1\, d_{yz}^1$, in which the unpaired electrons are coupled antiferromagnetically and ferromagnetically, respectively, see Figures 1 and 2.

The spin-density plot shown in Figure 2 indicates that $^{1,3}[(Py)_2Fe^{III}(OEPO^{\bullet})]^+$ in the open shell singlet and triplet states may be described as antiferro- and ferromagnetically coupled Fe^{III} (S = 1/2) $PO^{\bullet 2-}$ electronic configuration respectively.[52]

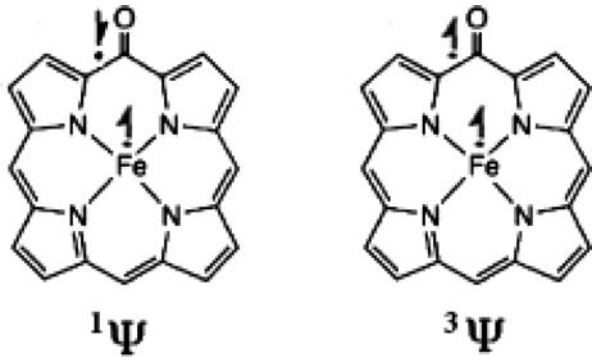

Figure 1. Two cartoons representing different electronic aspects of the $^{1,3}[(Py)_2Fe^{III}(PO^{\bullet})]^+$.

Data of Figure 1 and 2 suggest that $^{1,3}[(Py)_2Fe^{III}(PO^{\bullet})]^+$ are diradical species with two unpaired electrons. The electron and spin distributions for $[(Py)_2Fe^{III}(PO^{\bullet})]^+$, in the open-shell singlet state, are interesting. Table 3 shows that $[(Py)_2Fe^{III}(PO^{\bullet})]^+$ in the ground state has one unpaired electron on the iron (spin density 1.05) and the other single electron on the macrocycle (spin density −0.95) with antiparallel spin. This cation radical species is found to be EPR-silent[53] in coherence with this work. Spin contamination was assessed, and an $\langle S^2\rangle$ value of 1.15 was obtained for $^1[(Py)_2Fe^{III}(PO^{\bullet})]^+$. This value shows considerable spin contamination and is confirmatory of one unpaired electron on the iron that is considered as the d_{yz} iron orbital (Figure 3). However, there is around a 0.82 kcal/mol energy difference between the singlet and triplet states of $[(Py)_2Fe^{III}(PO^{\bullet})]^+$, which makes spin admixture a possibility. The $[(Py)_2Fe^{III}(PO^{\bullet})]^+$ in the open-shell antiferromagnetically coupled, with spin corrected energies (pure singlet), has been stabilized at 0.74 kcal/mol, which shows the increasing splitting of the singlet−triplet states. The closed shell diamagnetic form of $^1[(Py)_2Fe^{III}(PO^{\bullet})]^+$ with paired electronic configuration is considerably more destabilized (5.43 kcal/mol in the gas phase and 13.50 kcal/mol in the aqueous environment). Figure 3 depicts the last four HOMOs of the $^2[(Py)_2Fe^{III}(PO)]^0$ and $^{1,3}[(Py)_2Fe^{III}(PO^{\bullet})]^+$. Figure 3a shows that in the species $^2[(Py)_2Fe^{III}(PO)]^0$ (Table 3) the unpaired electron is localized completely on the iron d_{xy} orbital. Figure 3b shows that in species $^{1,3}[(Py)_2Fe^{III}(PO^{\bullet})]^+$, invariably, two unpaired electrons are π^*-type orbitals localized on the a_{2u} of macrocycle and iron d_{yz} with small tails to macrocycle atoms. Thus, the radical nature of the macrocycle in $[(Py)_2Fe^{III}(PO)]^0$ (at high temperatures)[33] and $[(Py)_2Fe^{III}(PO^{\bullet})]^+$ makes them air sensitive, and they readily undergo opening of the oxophlorin ligand to produce verdoheme.

Table 3. Calculated Mulliken Charges and Spin Densities for the Fe, O, C_{oxo}, C_{meso} Atoms and the Ring Macrocycle (Values in Parentheses Are Charge Densities)

compounds	Fe	ring	O	C_{oxo}	meso carbons	meso carbon trans
$^1[(Py)2\ Fe^{III}(PO)]^+$ closed-shell	(1.68)	(−0.67)	(−0.46)	(0.18)	(−0.10)	(0.08)
$^1[(Py)2\ Fe^{III}(PO^{\bullet})]^+$ open-shell	1.05 (1.57)	−0.95 (−0.57)	0.29 (−0.41)	0.15 (0.23)	0.13 (0.04)	0.27 (0.04)
$^2[(Py)2\ Fe^{III}(PO)]^0$	1.05 (1.57)	−0.03 (−1.56)	0.29 (−0.41)	0.15 (0.23)	0.13 (0.04)	0.27 (0.04)
$^1[(Py)2\ Fe^{II}(POH)]$	(1.22)	(−2.20)	(−0.56)	(0.19)	(−0.11)	(0.09)

dx.doi.org/10.1021/ic3017497 | Inorg. Chem. 2012, 51, 12857−12866

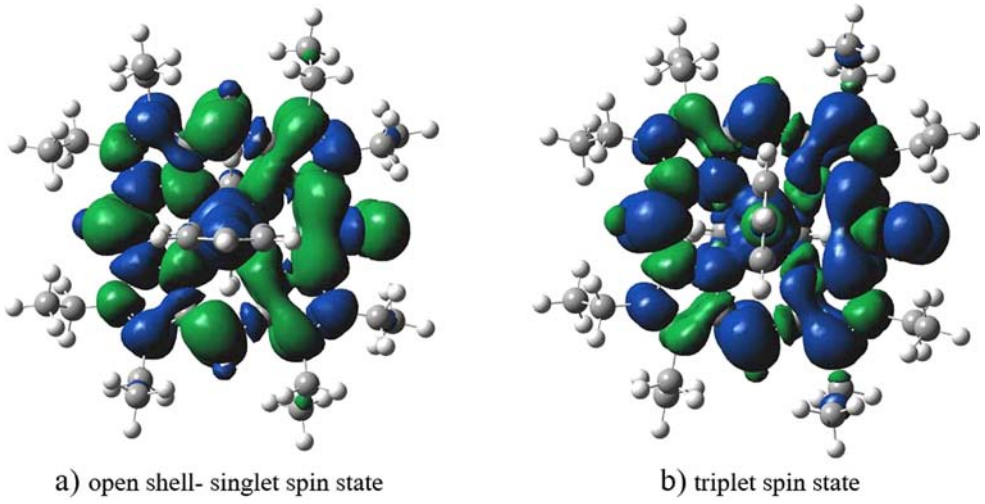

Figure 2. $^{1,3}[(Py)_2Fe^{III}(OEPO^{\bullet})]^{+}$: spin-density plot (majority spin in blue; minority spin in green).

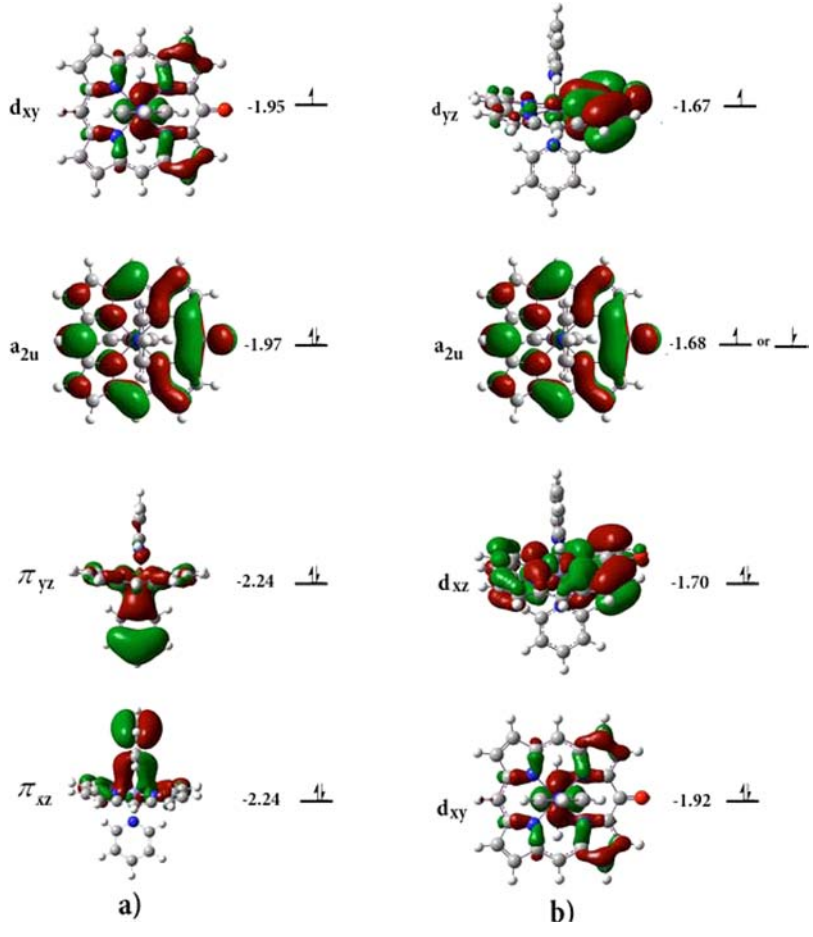

Figure 3. Kohn–Sham orbitals for the last 4 HOMOs of species (a) $^{2}[(Py)_2Fe^{III}(PO)]^{0}$ and (b) $^{1,3}[(Py)_2Fe^{III}(PO^{\bullet})]^{+}$.

To further confirm the electronic structures, we performed an NBO analysis for $[(Py)_2Fe^{III}(PO^{\bullet})]^{+}$. Table 4 shows the result of NBO analysis. The data in Table 4 indicate that the occupancy number of the alpha spin orbital for iron is 2.88 and that of the beta spin orbital of iron is 1.87, which results in a net alpha spin of 1.01 on the iron. In addition, one unpaired electron with beta orientation is present on the macrocycle to make the whole system a singlet open shell. The ^{1}H NMR of $[(Py)_2Fe\ (OEPO)]^{+}$ reported by Balch et al.[16] at −20 °C may be better clarified under the electron configuration resulted by this study. ^{1}H NMR spectra of $[(Py)_2Fe\ (OEPO)]^{+}$ nearly but not completely fall in the conventional diamagnetic region, but meso resonances occur at relatively upfield positions. They suggest that the species has a diamagnetic ground state with a nearby paramagnetic state. This study confirms that the ground state has a diradical nature that two unpaired electrons are strongly antiferromagnetically coupled. However, there is a nearby paramagnetic state around 1 kcal/mol above the singlet

dx.doi.org/10.1021/ic3017497 | *Inorg. Chem.* 2012, 51, 12857–12866

Table 4. NBO Analysis of Electron Distribution in Iron Atom of $[(Py)_2Fe^{III}(PO^{\bullet})]^+$

alpha spin orbital		beta spin orbital	
occupancy	orbital	occupancy	orbital
0.98726	LP (1)Fe	−0.93470	LP (1)Fe
0.98164	LP (2)Fe	−0.93922	LP (2)Fe
0.91010	LP (3)Fe		
sum of alpha spin electron		sum of beta spin electron	
2.87900		−1.87392	

states which contributes to the spin admixture and results in a partial paramagnetic character of this compound.

Parallel and perpendicular orientation of pyridines in $[(Py)_2Fe^{III}(PO^{\bullet})]^+$, in almost all spin states, are degenerate. There is, thus, no preference for parallel or perpendicular orientations of pyridines for $[(Py)_2Fe^{III}(PO^{\bullet})]^+$ (see Table 1). However, $[(Py)_2Fe^{III}(OEPO)]$ in a parallel orientation of the pyridines exists in the high spin state and in the perpendicular orientation in the low spin form.[20] According to present calculations, the crystal structure reported for $[(Py)_2Fe^{III}(OEPO)]$ which has parallel pyridines somehow fits better with the structure of oxidized species $[(Py)_2Fe^{III}(OEPO^{\bullet})]^+$. No practical barrier of rotation was found for axial pyridine ligands in the gas phase for $^{1,3}[(Py)_2Fe^{III}(PO^{\bullet})]^+$, while for $^{2}[(Py)_2Fe^{III}(PO)]^0$ (with intermediate π-accepting ability of axial pyridines and Fe−N_{ax} = 2.03 Å) the barrier of rotation for axial pyridine ligands in the gas phase is about 6.95 kcal/mol.[33] So a puzzle that remains to be answered is how the perpendicular oriented species in solution could be converted to its parallel counterpart via crystallization. Whether facile oxidation of $[(Py)_2Fe^{III}(OEPO)]$ by traces of O_2 leaks during the crystallization period caused the conversion of $[(Py)_2Fe^{III}(OEPO)]$ to $[(Py)_2Fe^{III}(OEPO^{\bullet})]^+$ or the change of orientation of pyridine in the solid state is the result of strong crystal packing forces still needs to be resolved. In this oxidized species with a high spin state and parallel pyridines, the calculated Fe−N_{ax} distance is 2.28 Å, and the average Fe−N_{eq} distance is 2.04 Å. There is good agreement with distances reported for the crystal structure of $[(Py)_2Fe^{III}(OEPO)]$ in which the Fe−N_{ax} distance is 2.26 Å and the average Fe−N_{eq} distance is 2.05 Å. Figure 3b demonstrates that in $^{1,3}[(Py)_2Fe^{III}(PO^{\bullet})]^+$ with pyridines in perpendicular orientation d_{xz} and d_{yz} orbitals of Fe do not have an effective overlap with π orbitals of pyridines. Hence, the axial Fe−N distance is increased (Fe−N_{ax} = 2.06 Å), and pyridines can readily rotate about the z axis (see Table 2).

$[(Py)_2Fe^{II}(POH)]$. The geometry and energy of six-coordinate $[(Py)_2Fe^{II}(POH)]$ have been fully optimized and computed with the pyridine groups in parallel and perpendicular planes in both singlet and triplet states. The singlet spin state (ground state) is 9.72 kcal/mol more stable than the triplet spin state at the OPBE/6-311+G** level, which is in good agreement with data reported by Balch and co-workers. They also found that in the solid state the pyridines are on parallel planes.[48] The key geometric parameters of the optimized structure for $[(Py)_2Fe^{II}(POH)]$ are collected in Table 2. The combined experimental−theoretical study of $[(Py)_2Fe^{II}(POH)]$ also shows that the observed structural parameters fit only those of the singlet spin state. Figure 4 shows an image of the structure from the data obtained by the OPBE method at a singlet spin state. (The data obtained by B3LYP are presented in the Supporting Information).

In the $[(Py)_2Fe^{II}(POH)]$ with parallel pyridines, the Fe−N_{ax} distance is 2.01 A°, and the average Fe−N_{eq} distance is 2.00 A°. In the crystal structure, the Fe−N_{ax} distance is 2.01 A°, the average Fe−N_{eq} distance is 1.99 A°, and the axial pyridines are parallel. In the $[(Py)_2Fe^{II}(POH)]$ with parallel pyridines, one of

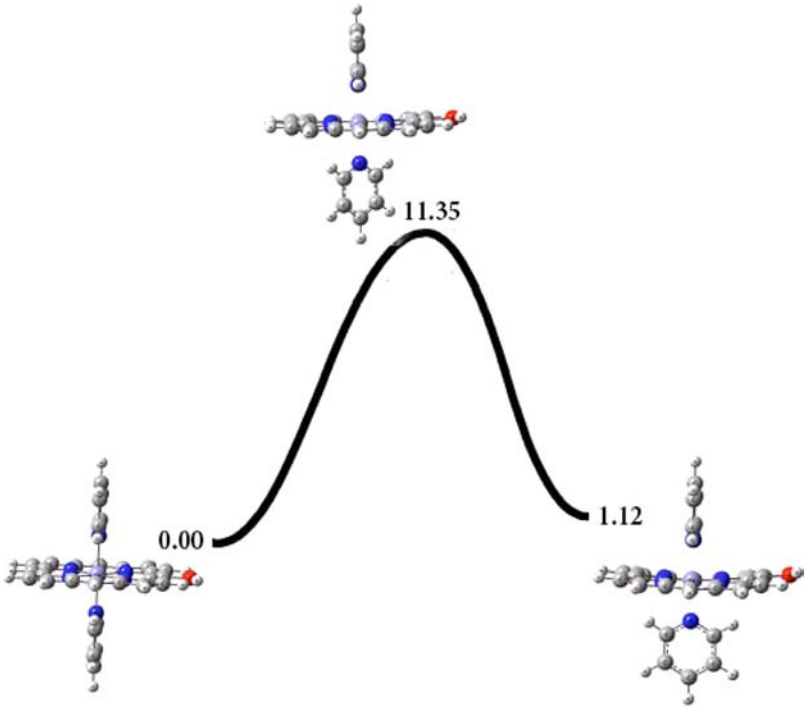

Figure 4. Energy diagram for conversion of $[(Py)_2Fe^{II}(POH)]$ with parallel pyridine to $[(Py)_2Fe^{II}(POH)]$ with perpendicular pyridine on the singlet surface.

dx.doi.org/10.1021/ic3017497 | Inorg. Chem. 2012, 51, 12857−12866

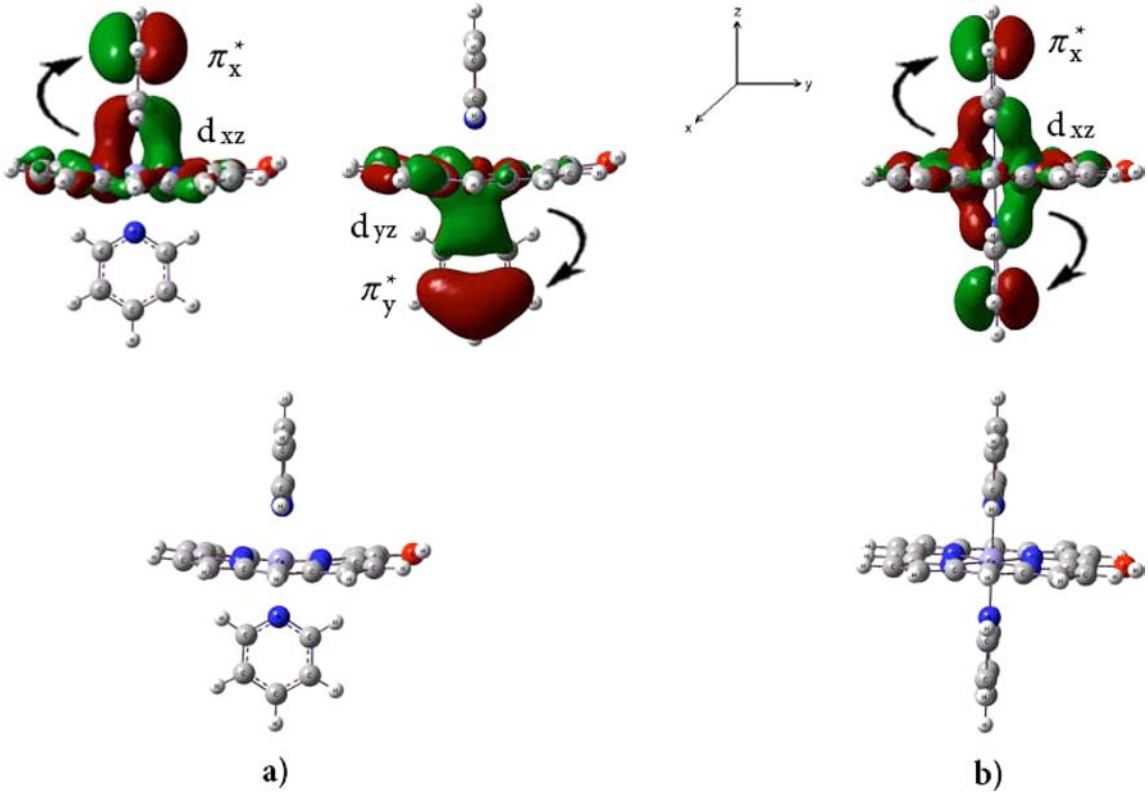

Figure 5. MO and KS, relevant to (a) perpendicular pyridines in $[(Py)_2Fe^{II}(POH)]$ and (b) parallel pyridines in $[(Py)_2Fe^{II}(POH)]$, with A symmetry.

the pyridines rotates around the z axis to produce two perpendicular pyridines in the $[(Py)_2Fe^{II}(POH)]$ complex that has been destabilized by about 1.12 kcal/mol. Our calculations in the gas phase show that a large barrier of rotation, 11.35 kcal/mol, is needed for the rotation of pyridines around the z axis on the singlet surface (see Figure 4). There is no difference in the preference for parallel or perpendicular orientations of pyridines for the low spin state because they have similar energies, and in the crystal structure, crystal forces cause a preference for parallel orientation and restrict the rotation of the pyridines toward perpendicular orientation. Since the β-ethyl groups of OEPOH were removed for the simplicity of calculation, we obtained rotation barrier of complex of $[(Py)_2Fe^{II}$ (OEPOH)] as well. The barrier of rotation was calculated to be 11.35 kcal/mol for $[(Py)_2Fe^{II}(POH)]$ and 11.50 kcal/mol for $[(Py)_2Fe^{II}(OEPOH)]$. Thus, substituted ethyls have no significant effect on the rotation barrier of axial ligands, possibly due to the large distance of ethyls from the metal center, see Figure S1.

Figure 5 demonstrates that in $[(Py)_2Fe^{II}(POH)]$ with perpendicular pyridines both of the degenerate orbitals d_{xz} and d_{yz} of Fe have an effective overlap with π_x* and π_y* acceptor orbitals of pyridines, respectively, and with parallel pyridines, the d_{xz} orbital of Fe has an effective overlap with the π_x* acceptor orbitals of pyridines. It has been found that in reduced species $[(Py)_2Fe^{II}(POH)]$, pyridines have a more π-accepting character and bind more tightly to iron. Due to this strong orbital overlap, the axial Fe−N distance is decreased (Fe−N_{ax} = 2.01 Å), and the complex of $^1[(Py)_2Fe^{II}(POH)]$ has the shortest axially bonded ligand to metal distance and the highest barrier of rotation (see Table 2). Therefore, pyridines cannot readily rotate around the z axis, and π-back-bonding to the acceptor pyridine ligands contributes to the stabilization of the low-spin Fe (II) state. Tight binding of the pyridine ligands in $[(Py)_2Fe^{II}(POH)]$ with an electronic configuration of $(\pi_{xz}\ \pi_{yz})^4\ a_{2u}{}^2\ d_{xy}{}^2$ may inhibit the access of dioxygen to the iron and render the complexes air stable. Once exposed to dioxygen, the reduced species immediately converts again to $[(py)_2Fe^{III}(OEPO)]$ as shown in the ^{1}H NMR spectrum reported by Rath et al., and heme degradation starts after that.[48,54] However, it seems that $[(Py)_2Fe^{III}(PO)]^0$ (at low temperatures) and $[(Py)_2Fe^{II}(POH)]$ should be considerably less reactive toward O_2 in heme degradation.

Redox Reactions of $[(Py)_2Fe^{III}(PO)]^0$ Complex. Electrochemical and theoretical studies reveal that $^2[(Py)_2Fe^{III}(PO)]^0$ undergoes two reversible,[16] one-electron transfer processes as outlined in Scheme 2.

Our calculations show that one-electron oxidation of $^2[(Py)_2Fe^{III}(PO)]^0$ with a $(\pi_{xz}\ \pi_{yz})^4\ a_{2u}{}^2\ d_{xy}{}^1$ electronic configuration to $^{1,3}[(Py)_2Fe^{III}(PO^{\bullet})]^+$ with a $d_{xy}{}^2\ d_{xz}{}^2\ a_{2u}{}^1\ d_{yz}{}^1$ electronic configuration takes place at low positive potentials in accordance with experimental results (with ionization energies = 3.95 kcal/mol). The oxidation of $^2[(Py)_2Fe^{III}(PO)]^0$ species by losing one electron from iron d orbitals is disfavored (with ionization energies = 21.15 kcal/mol) due to the high charge density of iron (1.57). Therefore, the computational study shows that $^2[(Py)_2Fe^{III}(PO)]^0$ is oxidized by losing one electron from its a_{2u} orbital, although d_{xy} and a_{2u} orbitals are almost degenerate. Due to this electron transfer mainly from the HOMO of the oxophlorin ring (a_{2u}), the charge density on the iron goes from $^2[(Py)_2Fe^{III}(PO)]^0$ to $^{1,3}[(Py)_2Fe^{III}(PO^{\bullet})]^+$ and remains fixed at around 1.57, which is consistent with the formation of an iron(III) oxidation state (see Table 3 and Figure 6).

dx.doi.org/10.1021/ic3017497 | Inorg. Chem. 2012, 51, 12857−12866

Scheme 2

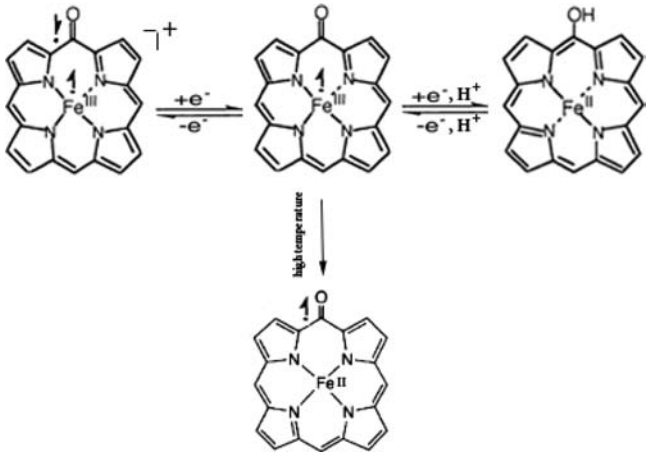

Our calculations show that one-electron reduction of dioxygen takes place at a positive potential (with reduction potential energies in the gas phase = 14.17 kcal/mol). Hence, oxidation of $[(Py)_2Fe^{III}(PO)]^0$ occurs in the presence of dioxygen. This explains why the complex of $[(Py)_2Fe^{III}(OEPO)]^0$ is so unstable in the air and is readily oxidized. Therefore, in the coupled oxidation process in pyridine, it is possible for a dioxygen to convert $[(Py)_2Fe^{III}(OEPO)]^0$ into $[(Py)_2Fe^{III}(OEPO^{\bullet})]^+$ before further oxidation at the meso carbon occurs.

Subsequently, the reduced form of $^1[(Py)_2Fe^{II}(PO)]^-$ with a $(\pi_{xz}\,\pi_{yz})^4\,d_{xy}^2$ electronic configuration is formed by the addition of an electron to the d_{xy} SOMO orbital of $^2[(Py)_2Fe^{III}(PO)]^0$. Then, the reduced form is easily protonated to the hydroxy form of $^1[(Py)_2Fe^{II}(POH)]$. This reduction takes place at low potentials (with reduction energies = −32.06 kcal/mol). Due to this electron transfer mainly on the iron, the charge density on the iron decreases from around 1.57 in $^2[(Py)_2Fe^{III}(PO)]^0$ to 1.22 in $^1[(Py)_2Fe^{II}(POH)]$, which is better viewed as Fe(II) d^6 with the macrocycle as a trianionic (see Table 3). These results indicate that $[(Py)_2Fe^{III}(PO)]^0$ undergoes oxidation to form a monocation and a reduction to form a hydroxy. Such a fact corroborates well with the electrochemical data reported for $[(py)_2Fe(OEPO)]$ by Balch et al.[16,20] Interestingly, the identity of the SOMO and HOMO of the $[(py)_2Fe(OEPO)]$ suggests the sites of oxidation and reduction and the electronic structures of oxidized and reduced forms.

Theoretical studies show that $[(Py)_2Fe^{III}(PO^{\bullet})]^+$ has an open-shell singlet ground state with two unpaired electrons on the iron and the macrocycle with antiparallel spin, making it a highly reactive species in the heme degradation process. Consequently, theoretical data reveal that $[(Py)_2Fe^{III}(OEPO^{\bullet})]^+$ has a significant role in heme destruction. On the contrary, $[(Py)_2Fe^{II}(POH)]$ with a strong π-interaction between Fe(II) and the pyridine axial ligands and an electronic configuration of $(\pi_{xz}\,\pi_{yz})^4\,a_{2u}^2\,d_{xy}^2$ does not have a significant role in this process. Calculation data also show that in the couple oxidation, complex $[(Py)_2Fe^{III}(OEPO)]^0$ is susceptible to inhibition by reductant agents.

Ortiz de Montellano[13] and Morishima et al.[55] showed and discussed that the minimal mechanism for the conversion of α-meso-hydroxyheme to verdoheme requires deprotonation of α-meso-hydroxyheme to form a reactive iron oxophlorin, which is in very good agreement with the theoretical data in this work.

The Relevancy of Oxidation Number of Fe with Crossover Spins Property. The structures, HOMO−LUMO energies, and associated gaps for $[(Py)_2Fe^{III}(PO^{\bullet})]^+$, $[(Py)_2Fe^{III}(PO)]^0$, and $[(Py)_2Fe^{II}(POH)]$ are given at the B3LYP/6-311+G** level. The calculated HOMO and LUMO energies and associated gaps complement the experimental results obtained via electrochemical studies.

Figure 6 presents the ground state frontier MO energy diagrams for the above complexes. The pyridine axial ligand acts as a σ donator to Fe(III) in $[(Py)_2Fe^{III}(PO^{\bullet})]^+$ and causes this complex to adopt the $d_{xy}^2\,(d_{xz}\,d_{yz})^3$ ground state with a low energy gap and low lying exited states. In $[(Py)_2Fe^{III}(PO)]^0$ and $[(Py)_2Fe^{II}(POH)]$, with much better π-accepting ability of the pyridine ligands, the ground state $(\pi_{xz}\,\pi_{yz})^4\,d_{xy}^2$ electronic configuration was obtained, but the energy gap between the d_{xy} and d_π orbitals of Fe(II) in $[(Py)_2Fe^{II}(PO)]^-$ is larger than

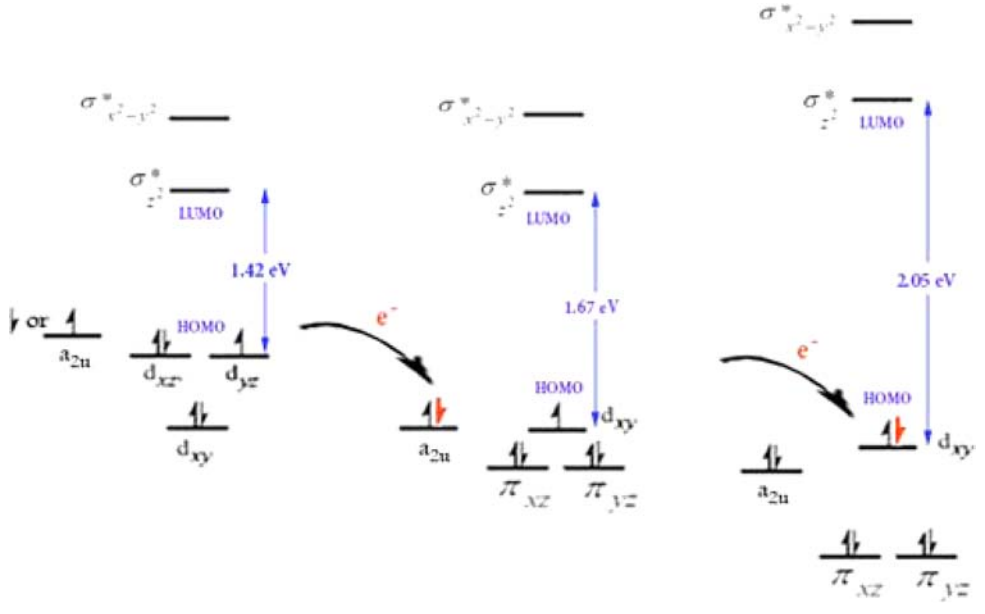

Figure 6. Redox reaction of $^2[(Py)_2Fe^{III}(PO)]^0$ with the electronic configuration in low spin states and a HOMO−LUMO gap.

dx.doi.org/10.1021/ic3017497 | Inorg. Chem. 2012, 51, 12857−12866

Fe(III) in $[(Py)_2Fe^{III}(PO)]^0$. Figure 6 also shows that the HOMO−LUMO gaps of $[(Py)_2Fe^{III}(PO^{\bullet})]^+$ (1.42 eV), $[(Py)_2Fe^{III}(PO)]^0$ (1.67 eV), and $[(Py)_2Fe^{II}(POH)]$ (2.05 eV) span a remarkably wide range of about 0.63 eV. These results provide some of the first insights into just how dramatically the axial ligands[33] and oxidation number of metal can tune the HOMO−LUMO gaps and hence the spin state energy of iron oxophlorin complexes. The HOMO−LUMO gaps provide a qualitative explanation of why the experimental analogue of $[(Py)_2Fe^{III}(OEPO^{\bullet})]^+$ which has low-energy excited states with (s = 2) exhibits spin crossover behavior with the temperature.[16] The diagram presented in Figure 6 also indicates why such behavior would be out of the question for reduced species $[(Py)_2Fe^{II}(OEPO)]^-$ or $[(Py)_2Fe^{II}(POH)]$, and latter species are diamagnetic and temperature invariant and consistent with a closed-shell singlet state.

Careful examination of the MO occupancies reveals a somewhat subtle point, that the lowest energy quintet derives from a $d_{xz}\rightarrow\sigma^*_{z^2}$ excitation, rather than from a $d_{xy}\rightarrow\sigma^*_{z^2}$ excitation. Approximately, the electronic configuration of the lowest-energy s = 2 state (quintet spin state) of $[(Py)_2Fe^{III}(PO^{\bullet})]^+$ may be described as follows: $d_{xy}^2\ d_{xz}^1\ a_{2u}^1\ d_{yz}^1\ \sigma^*_{z^2}{}^1$. In summary, the oxidation number of Fe has a major effect on the high-lying occupied and low-lying virtual orbitals, whereby the orbital energy levels shift in energy depending on the metal oxidation number. As the latter orbital is the HOMO, this also affects the electron abstraction ability of the oxidant.

Axial Ligand Effect on the Redox Reactions of Iron Oxophlorin. Recent studies on the reactivity of oxophlorin showed a dramatic axial ligand effect on the high-lying occupied and low-lying virtual orbitals of $[L_2Fe(PO)]^0$, whereby the orbital energy levels shift in energy depending on the nature of the axial ligand.[19,20,33] Here, an attempt has been made to shed more light on the axial ligand effect. To that effect, the structure, HOMO−LUMO energies, and associated gap at the OPBE/6-31+G* level for $[L_2Fe(PO)]^0$ (L = Im, Py, *t*-BuNC) in all possible spin states and different oxidation numbers have been calculated. Full details of these calculations are given in the Supporting Information, while only major trends have been focused on here.

In this work, our calculations show that one-electron oxidation of $[(Im)_2Fe^{III}(PO)]$ to $[(Im)_2Fe^{III}(PO)]^+$ takes place at low positive potentials (with ionization energies = 3.08 kcal/mol). A computational study shows that $[(Im)_2Fe^{III}(PO)]$ is oxidized by losing one electron from its a_{2u} orbital. Subsequently, the complex of $[(Im)_2Fe^{II}(POH)]$ is formed by the addition of one electron to the π_{xz} orbital of $[(Im)_2Fe^{III}(PO)]$ and one H^+; this reduction takes place at low potentials (with reduction energies = −17.35 kcal/mol). Thus, as shown in Table 5, the relatively smaller HOMO−LUMO gap of $[(Im)_2Fe^{III}(PO)]$ (1.39 eV) compared to that of $[(Py)_2Fe^{III}(PO)]$ (1.67 eV) and $[(t\text{-BuNC})_2Fe^{II}(PO^{\bullet})]$ (2.54 eV) is ascribed to the much higher HOMO energy level of $[(Im)_2Fe^{III}(PO)]$. Table 5 also shows the HOMO and LUMO energies and HOMO−LUMO gap of $[(Im)_2Fe^{III}(PO)]$, $[(Py)_2Fe^{III}(PO)]$, and $[(t\text{-BuNC})_2Fe^{II}(PO^{\bullet})]$.

Table 5. Calculated HOMO−LUMO Gap of Iron Oxophloin Complexes

	HOMO [eV]	LUMO [eV]	ΔE [eV]
$[(Py)_2Fe^{III}(PO^{\bullet})]^+$	−1.68	−0.26	1.42
$[(Py)_2Fe^{III}(PO)]^0$	−1.95	−0.28	1.67
$[(Py)_2Fe^{II}(POH)]$	−2.01	+0.04	2.05
$[(Im)_2Fe^{III}(PO)]^0$	−1.73	−0.34	1.39
$[(t\text{-BuNC})_2Fe^{II}(PO^{\bullet})]^0$	−2.06	+0.48	2.54

The nature of the axial ligand significantly influences the potential of both the oxidation and the reduction of these oxophlorin complexes. This result confirms that changing the electron affinity of the acceptors in axial ligands could effectively modulate the HOMO−LUMO gaps. Hence, complexes $[(Im)_2Fe^{III}(PO)]$ and $[(Py)_2Fe^{III}(PO)]$ both undergo auto-oxidation in the presence of dioxygen and remarkable reversible oxidation and reduction processes, while complex $[(t\text{-BuNC})_2Fe^{II}(PO^{\bullet})]$ undergoes an irreversible redox processes. The HOMO−LUMO gaps in these complexes are increased by an increase in the π-acceptor properties of Im < Py < *t*-BuNC. Complex $[(t\text{-BuNC})_2Fe^{II}(PO^{\bullet})]$ possesses relatively high LUMO energies ($\sigma^*_{x^2-y^2}$ = +0.48 eV) and low HOMO energies (d_{xy} = −2.06 eV), compared to $[(Im)_2Fe^{III}(PO)]$ and $[(Py)_2Fe^{III}(PO)]$ (see Table 5). The cyclic voltammograms of $[(Im)_2Fe^{III}(OEPO)]$ and $[(Py)_2Fe^{III}(OEPO)]$ show that they both undergo facile oxidation to form a monocation and a reduction to form an anion.[16,18] The nature of the axial ligand significantly influences the potential energy surfaces of HOMO and LUMO of the oxophlorin complexes.

In the gas phase, all of the oxidation and reduction processes are endothermic and exothermic, respectively. $[(Im)_2Fe^{III}(PO)]$ and $[(Py)_2Fe^{III}(PO)]$ have similar oxidation potentials, 48.77 and 52.83 kcal/mol, respectively, but $[(t\text{-BuNC})_2Fe^{II}(PO^{\bullet})]$ has a high positive oxidation potential (ΔG = 126.83 kcal/mol; see Figure 7).

The Solvent Effect on Redox Potentials. The importance of solvation on charged species is well recognized in the field. All of the detailed data are summarized in the Supporting Information (SI), while key results are discussed here.

Figure 7 shows the results in a pictorial manner, where one can discern the significant difference between the gas-phase and solution behavior. In the gas phase, all of the oxidation processes are highly endothermic, and the reduction processes are exothermic. This trend makes sense since charge−charge repulsion and attraction dominate in the gas phase and will strongly disfavor the oxidation and reduction of $[(L)_2Fe(PO)]$ species. However, as can be seen in Figure 7, in solution, all of the oxidation processes are facilitated due to a lower oxidation potential. The data for one electron oxidation of $[L_2Fe^{III}(PO)]$ to $[L_2Fe^{III}(PO^{\bullet})]^+$ show a much lower endothermic process ranging from 11.52 to 55.90 kcal/mol in acetonitrile and from 3.08 to 51.65 kcal/mol in H_2O. In the gas phase, oxidations are highly endothermic, ranging from 48.77 to 126.83 kcal/mol. Thus, as has been recognized before, solvation exerts a strong impact on the charge density of iron and the macrocycle in complexes $[L_2Fe^{III}(PO)]^+$. The solvent levels the oxidation potentials of all of the species by preferentially stabilizing the oxidized species $[L_2Fe^{III}(PO^{\bullet})]^+$. Therefore, in the solvent phase, the oxidation of the parent $[L_2Fe^{III}(PO)]$ species is considerably more facile than that of the gas phase.

The oxidized species $^1[L_2Fe^{III}(PO^{\bullet})]^+$ (open-shell) is more polar than $^1[L_2Fe^{III}(PO^{\bullet})]^+$ (closed-shell). Therefore, in polar solvents of H_2O, the species $^1[(Py)_2Fe^{III}(PO^{\bullet})]^+$ (open-shell) is much more stable than $^1[(Py)_2Fe^{III}(PO^{\bullet})]^+$ (closed-shell). Hence, the open shell−closed shell splitting in the gas phase is

dx.doi.org/10.1021/ic3017497 | Inorg. Chem. 2012, 51, 12857−12866

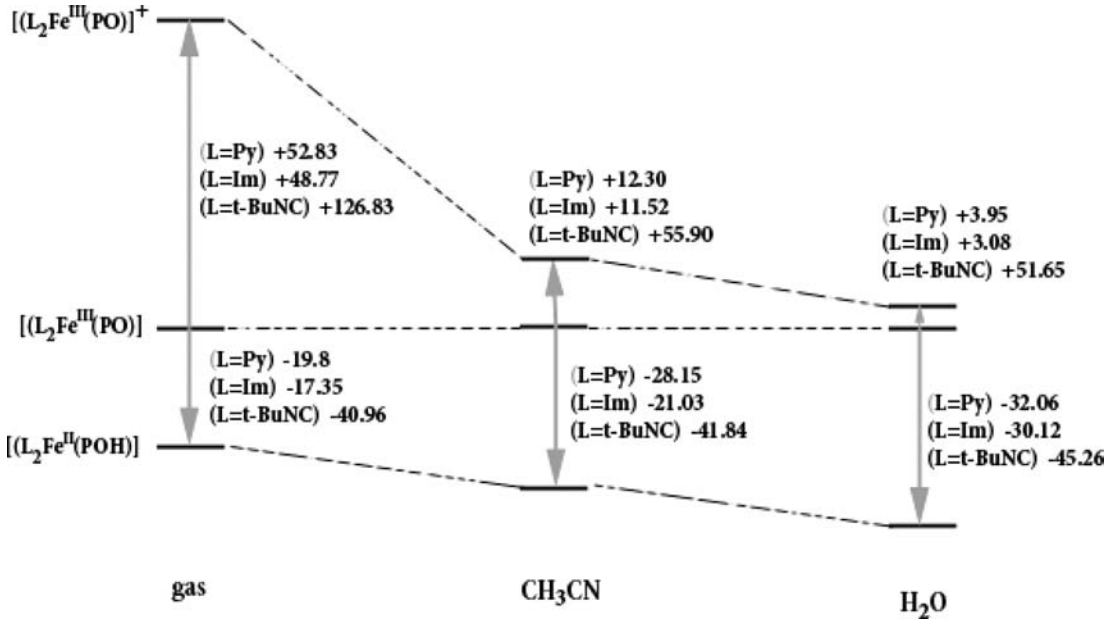

Figure 7. Schematic representation of solvent effect on oxidation and reduction potentials in kcal/mol.

5.43 kcal/mol, while in the H_2O phase, it is 13.50 kcal/mol (see Table 1).

CONCLUSION

The oxidation number of iron oxophlorin has profound effects on the electronic configuration, spin states, and reactivity of the iron oxophlorins.

The iron oxophlorin six-coordinate complex, $[(Py)_2Fe^{III}(PO)]^0$, undergoes two reversible, one-electron transfer processes. $[(Py)_2Fe^{III}(PO)]^0$ loses one electron from its a_{2u} readily by auto-oxidation with O_2. This oxidized species, $[(Py)_2Fe^{III}(PO^{\bullet})]^+$, has the open-shell-singlet ground state d_{xy}^2 d_{xz}^2 a_{2u}^1 d_{yz}^1 electronic configuration with closely lying triplet and quintet states. In $[(Py)_2Fe^{III}(PO^{\bullet})]^+$, iron is still in the +3 oxidation state and the macrocycle has a dianion radical nature. Either in the singlet or triplet states $^{1,3}[(Py)_2Fe^{III}(PO^{\bullet})]^+$ has a diradical nature that makes it quite reactive toward dioxygen by a spin allowed path. Subsequently, the complex $[(Py)_2Fe^{II}(POH)]$ with the $(\pi_{xz}\ \pi_{yz})^4$ a_{2u}^2 d_{xy}^2 electronic configuration is formed by the addition of one electron and proton to $^2[(Py)_2Fe^{III}(PO)]^0$. When Fe is in an oxidation state of +2, the axial pyridines are strong π acceptor such as $[(Py)_2Fe^{II}(POH)]$; the complex is diamagnetic, and its reaction with O_2 is spin forbidden.

The nature of the axial ligand significantly influences the potential of both the oxidation and the reduction of these oxophlorin complexes. The complexes $[(Im)_2Fe^{III}(PO)]$ and $[(Py)_2Fe^{III}(PO)]$ show that they both undergo facile oxidation to form a monocation and a reduction to form an anion while the $[(t\text{-BuNC})_2Fe^{II}(PO^{\bullet})]$ undergoes difficult oxidation processes indicating good correlation with the π-back-bonding ability of the *t*-BuNC ligand.

In conclusion, we found that oxidized species $[(Py)_2Fe^{III}(PO^{\bullet})]^+$ is essential for the following reaction with O_2 to yield verdoheme and to cleave the porphyrin ring because $[(Py)_2Fe^{III}(PO^{\bullet})]^+$ is highly reactive toward O_2, while reduced species $[(Py)_2Fe^{II}(POH)]$ is unreactive with O_2 in the heme degradation in the coupled oxidation state. In the solution phase, the heme catabolism process is facilitated due to lower oxidation potential. The conclusions drawn from calculations on the bis-pyridine and bis-imidazole complexes probably cannot be directly applicable to the hemeoxygenase studies, which is under study in our group.

ASSOCIATED CONTENT

Supporting Information

Tables include the iron-oxophlorin compound optimized *xyz* Cartesian coordinate data in different spin states. For each table, the corresponding figure is included. This material is available free of charge via the Internet at http://pubs.acs.org.

AUTHOR INFORMATION

Corresponding Author

*E-mail: n-safari@sbu.ac.ir. Tel.: + 98-21-22401765. Fax: + 98-21-22403041.

Notes

The authors declare no competing financial interest.

ACKNOWLEDGMENTS

We are grateful to Prof. S. W. Ng for providing us the Gaussian suite of programs and hardware (machine time) facilities and also making available to us the opportunity to access some new features of Gaussian products. The authors would like to acknowledge financial support from the Research Council of Shahid Beheshti University. Also technical support of the Chemistry Computational Center at Shahid Beheshti University is greatly acknowledged.

REFERENCES

(1) Ortiz de Montellano, P. R. In *The Porphyrin Handbook. Heme oxygenase structure and function*; Kadish, K. M., Smith, K. M., Guilard, R., Eds.; Academic Press: New York, 2003; Vol. *12*, Chapter XX, pp 183−210.

(2) Sono, M.; Roach, M. P.; Coulter, E. D.; Dawson, J. H. *Chem. Rev.* **1996**, *96*, 2841−2888.

(3) Yoshida, T.; Noguchi, M.; Kikuchi, G. *J. Biol. Chem.* **1980**, *255*, 4418−4420.

(4) Kikuchi, G.; Yoshida, T. *Trends Biochem. Sci.* **1980**, *5*, 323−325.

(5) Yoshida, T.; Migita, C. T. *J. Inorg. Biochem.* **2000**, *82*, 33−41.
(6) Rivera, M.; Zeng, Y. *J. Inorg. Biochem.* **2005**, *99*, 337−354.
(7) Balch, A. L.; Latos-Grazynski, L.; Noll, B. C.; Olmstead, M. M.; Szterenberg, L.; Safari, N. *J. Am. Chem. Soc.* **1993**, *115*, 1422−1429.
(8) Balch, A. L.; Latos-Grazynski, L.; Noll, B. C.; Olmstead, M. M.; Safari, N. *J. Am. Chem. Soc.* **1993**, *115*, 9056−9061.
(9) Hildebrand, D. P.; Tang, H.-l.; Luo, Y.; Hunter, C. L.; Smith, M.; Brayer, G. D.; Mauk, A. G. *J. Am. Chem. Soc.* **1996**, *118*, 12909−12915.
(10) Bonnett, R.; Dimsdale, M. J. *J. Chem. Soc., Perkin Trans. 1* **1972**, 2540−2548.
(11) Fuhrhop, J. H.; Besecke, S.; Subramanian, J. *J. Chem. Soc., Chem. Commun.* **1973**, 1−2.
(12) Balch, A. L. *Coord. Chem. Rev.* **2000**, *200*−*202*, 349−377.
(13) Ortiz de Montellano, P. R. *Acc. Chem. Res.* **1998**, *31*, 543−549.
(14) Kumar, D.; Visser, S.; Shaik, S. *J. Am. Chem. Soc.* **2005**, *127*, 8204−8213.
(15) Balch, A. L.; Latos-Grażyński, L.; Noll, B. C.; Szterenberg, L.; Zovinka, E. P. *J. Am. Chem. Soc.* **1993**, *115*, 11846−11854.
(16) Balch, A. L.; Koerner, R.; Latos-Grażyński, L.; Noll, B. C. *J. Am. Chem. Soc.* **1996**, *118*, 2760−2761.
(17) Kalish, H.; Camp, J. E.; Stępień, M.; Latos-Grażyński, L.; Balch, A. L. *J. Am. Chem. Soc.* **2001**, *123*, 11719−11727.
(18) Rath, S. P.; Olmstead, M. M.; Balch, A. L. *Inorg. Chem.* **2004**, *43*, 7648−7655.
(19) Rath, S. P.; Olmstead, M. M.; Balch, A. L. *J. Am. Chem. Soc.* **2004**, *126*, 6379−6386.
(20) Rath, S. P.; Olmstead, M. M.; Balch, A. L. *Inorg. Chem.* **2006**, *45*, 6083−6093.
(21) Zhang, X.; Fujii, H.; Matera, K. M.; Migita, C. T.; Sun, D.; Sato, M.; Ikeda-Saito, M.; Yoshida, T. *Biochemistry* **2003**, *42*, 7418−7426.
(22) Lad, L.; Friedman, J.; Li, H.; Bhaskar, B.; Ortiz de Montellano, P. R.; Poulos, T. L. *Biochemistry* **2004**, *43*, 3793−3801.
(23) Matsui, T.; Unno, M.; Ikeda-Saito, M. *Acc. Chem. Res.* **2009**, *43*, 240−247.
(24) Tanaka, R.; Kowase, S.; Unno, M. *Dalton Trans.* **2010**, *39*, 9235−9237.
(25) Bahrami, H.; Zahedi, M.; Safari, N. *J. Inorg. Biochem.* **2006**, *100*, 1449−1461.
(26) Gheidi, M.; Safari, N.; Bahrami, H.; Zahedi, M. *J. Inorg. Biochem.* **2007**, *101*, 385−395.
(27) Jamaat, P.; Safari, N.; Ghiasi, M.; Naghavi, S.; Zahedi, M. *J. Biol. Inorg. Chem.* **2008**, *13*, 121−132.
(28) Gheidi, M.; Safari, N.; Zahedi, M. *J. Mol. Model.* **2010**, *16*, 1401−1413.
(29) Lai, W.; Chen, H.; Matsui, T.; Omori, K.; Unno, M.; Ikeda-Saito, M.; Shaik, S. *J. Am. Chem. Soc.* **2010**, *132*, 12960−12970.
(30) Mansfield Matera, K.; Takahashi, S.; Fujii, H.; Zhou, H.; Ishikawa, K.; Yoshimura, T.; Rousseau, D. L.; Yoshida, T.; Ikeda-Saito, M. *J. Biol. Chem.* **1996**, *271*, 6618−6624.
(31) Liv, Y.; Moenne-Loccoz, P.; Loehr, T. M.; Ortiz de Montellano, P. R. *J. Biol. Chem.* **1997**, *272*, 6909−6917.
(32) Sakamoto, H.; Omata, Y.; Palmer, G.; Noguchi, M. *J. Biol. Chem.* **1999**, *274*, 18196−18200.
(33) Gheidi, M.; Safari, N.; Zahedi, M. *Inorg. Chem.* **2012**, *51*, 7094−7102.
(34) Siegbahn, P. E. M. *Faraday Discuss.* **2003**, *124*, 289−296.
(35) Frisch, M. J.; Trucks, G. W.; Schlegel, H. B.; Scuseria, G. E.; Robb, M. A.; Cheeseman, J. R.; Zakrzewski, V. G.; Montgomery, J. A.; Stratmann, R. E.; Burant, J. C.; Dapprich, S.; Millam, J. M.; Daniels, A. D.; Kudin, K. N.; Strain, M. C.; Farkas, O.; Tomasi, J.; Barone, V.; Cossi, M.; Cammi, R.; Mennucci, B.; Pomelli, C.; Adamo, C.; Clifford, S.; Ochterski, J.; Petersson, G. A.; Ayala, P. Y.; Cui, Q.; Morokuma, K.; Malick, D. K.; Rabuck, A. D.; Raghavachari, K.; Foresman, J. B.; Cioslowski, J.; Ortiz, J. V.; Stefanov, B. B.; Liu, G.; Liashenko, A.; Piskorz, P.; Komaromi, I.; Gomperts, R.; Martin, R. L.; Fox, D. J.; Keith, T.; Al-Laham, M. A.; Peng, C. Y.; Nanayakkara, A.; Ghonzalez, C. V.; Challacombe, M. W.; Gill, P. M.; Johnson, B. G.; Chen, W.; Wong, M.; Andres, J. L.; Head-Gordon, M.; Replogle, E. S.; Pople, J. A. *Gaussian 03*, revision A.1; Gaussian, Inc.: Pittsburgh, PA, 2003.
(36) Parr, R. G.; Yang, W. *Density-Function Theory of Atoms and Molecules*; Oxford University Press: Oxford, U. K., 1989.
(37) Cramer, C. J. *Essentials of Computational Chemistry: Theories and Models*, Wiley: Chichester, U. K., 2002.
(38) Swart, M. *J. Chem. Theory Comput.* **2008**, *4*, 2057−2066.
(39) Güell, M.; Luis, J. M.; Solá, M.; Swarta, M. *J. Phys. Chem. A* **2008**, *112*, 6384−6391.
(40) Lee, C.; Yang, W.; Parr, R. G. *Phys. Rev. B* **1988**, *37*, 785−789.
(41) Vosko, S. H.; Wilk, L.; Nusair, M. *Can. J. Phys.* **1980**, *58*, 1200−1211.
(42) Stephens, P. J.; Devlin, F. J.; Chabalowski, C. F.; Frisch, M. J. *J. Phys. Chem.* **1994**, *98*, 11623−11627.
(43) Yoshizawa, K.; Kamachi, T.; Shiota, Y. *J. Am. Chem. Soc.* **2001**, *123*, 9806−9816.
(44) Shiota, Y.; Yoshizawa, K. *J. Am. Chem. Soc.* **2000**, *122*, 12317−12326.
(45) Wittbrodt, J. M.; Schlegel, H. B. *J. Chem. Phys.* **1996**, *105*, 6574−6577.
(46) Groenhof, A. R.; Swart, M.; Ehlers, A. W.; Lammertsma, K. *J. Phys. Chem. A* **2005**, *109*, 3411−3417.
(47) Wong, M. W.; Frisch, M. J.; Wiberg, K. B. *J. Am. Chem. Soc.* **1992**, *114*, 1645−1652.
(48) Rath, S. P.; Olmstead, M. M.; Balch, A. L. *Inorg. Chem.* **2004**, *43*, 6357−6365.
(49) Ghosh, A. *J. Biol. Inorg. Chem.* **2006**, *11*, 671−673.
(50) Ghosh, A. *J. Biol. Inorg. Chem.* **2006**, *11*, 712−724.
(51) Tangen, E.; Conradie, J.; Ghosh, A. *J. Chem. Theory Comput.* **2007**, *3*, 448−457.
(52) Wasbotten, I.; Ghosh, A. *Inorg. Chem.* **2006**, *45*, 4914−4921.
(53) Migita, C. T.; Migita, H.; Mansfield Matera, K.; Takahashi, S.; Zhou, H.; Yoshida, T. *Biochim. Biophys. Acta* **1999**, *1432*, 203−213.
(54) Rath, S. P. *J. Chem. Sci.* **2006**, *118*, 463−474.
(55) Morishima, I.; Fujii, H.; Shiro, Y.; Sano, S. *Inorg. Chem.* **1995**, *34*, 1528−1535.